


Cite this: *RSC Adv.*, 2022, 12, 26588

# A first-principles investigation of the linear thermal expansion coefficients of BeF<sub>2</sub>: giant thermal expansion

Chee Kwan Gan,<sup>a</sup> Abdullah I. Al-Sharif,<sup>b</sup> Ammar Al-Shorman<sup>b</sup> and Abdallah Qteish<sup>\*b</sup>

We present the results of a theoretical investigation of the linear thermal expansion coefficients (TECs) of BeF<sub>2</sub>, within a direct Grüneisen formalism where symmetry-preserving deformations are employed. The required physical quantities such as the optimized crystal structures, elastic constants, mode Grüneisen parameters, and phonon density of states are calculated from first-principles. BeF<sub>2</sub> shows an extensive polymorphism at low pressures, and the lowest energy phases [ $\alpha$ -cristobalite with space group (SG) *P*4<sub>1</sub>2<sub>1</sub>2 and its similar phase with SG *P*4<sub>3</sub>2<sub>1</sub>2] are considered in addition to the experimentally observed  $\alpha$ -quartz phase. For benchmarking purposes, similar calculations are performed for the rutile phase of ZnF<sub>2</sub>, where the volumetric TEC ( $\alpha_v$ ), derived from the calculated linear TECs along the *a* ( $\alpha_a$ ) and *c* ( $\alpha_c$ ) directions, is in very good agreement with experimental data and previous theoretical results. For the considered phases of BeF<sub>2</sub>, we do not find any negative thermal expansion (NTE). However we observe diverse thermal properties for the distinct phases. The linear TECs are very large, especially  $\alpha_c$  of the  $\alpha$ -cristobalite phase and its similar phase, leading to giant  $\alpha_v$  ( $\sim 175 \times 10^{-6} \text{ K}^{-1}$  at 300 K). The giant  $\alpha_v$  arises from large Grüneisen parameters of low-frequency phonon modes, and the *C*<sub>13</sub> elastic constant that is negatively signed and large in magnitude for the  $\alpha$ -cristobalite phase. The elastic constants, high-frequency dielectric constants, Born effective charge tensors, and thermal properties of the above phases of BeF<sub>2</sub> are reported for the first time and hence serve as predictions.

Received 5th August 2022  
Accepted 9th September 2022

DOI: 10.1039/d2ra04860d

rsc.li/rsc-advances

## 1. Introduction

Beryllium fluoride (BeF<sub>2</sub>) is known to exist in glass and crystalline phases and has a variety of technological applications. BeF<sub>2</sub> glass has a large bandgap of about 13.8 eV, the lowest refractive index and highest Abbe number of any inorganic material, and exceptional resistance to damage. These properties have enabled the manufacturing of special glasses (from BeF<sub>2</sub> and its mixtures with fluorides and other difluorides) that have excellent transmittance in the UV region<sup>1,2</sup> and for use in high-power laser systems.<sup>3</sup> The LiF–BeF<sub>2</sub> mixture is a primary coolant and fuel solvent in molten salt nuclear reactors.<sup>4</sup> In protein crystallography, BeF<sub>2</sub> is used to restrict protein motion to facilitate the crystallography process.<sup>5</sup> Very recently, crystalline BeF<sub>2</sub> is predicted to be a better neutron filter than MgF<sub>2</sub>, which has been considered an effective neutron filter candidate.<sup>6</sup> The main aim of this work is to investigate, for the first time, the linear thermal expansion coefficients (TECs) of a few low-energy crystalline phases of BeF<sub>2</sub>. We also consider

a benchmark system ZnF<sub>2</sub> that has exceptional electric and optical properties, and interesting technological applications ranging from catalysis to spectroscopy and laser applications.<sup>7</sup>

Single crystal BeF<sub>2</sub> has been grown and found to have a crystal structure remarkably similar to that of the  $\alpha$ -quartz (SiO<sub>2</sub>) structure,<sup>8</sup> which has a trigonal symmetry with space group (SG) *P*3<sub>1</sub>21 (#152). A recent first-principles study has revealed that BeF<sub>2</sub> shows extensive polymorphism at low pressures.<sup>9</sup> Interestingly, three crystal phases [namely, (i) the  $\alpha$ -cristobalite phase that has a tetragonal symmetry with SG *P*4<sub>1</sub>2<sub>1</sub>2 (#92), (ii) a similar phase to the  $\alpha$ -cristobalite phase (hereafter referred to as the  $\alpha'$ -cristobalite phase) with SG *P*4<sub>3</sub>2<sub>1</sub>2 (#96), and (iii) the *C*2/*c*-2  $\times$  4 phase with SG *C*12/*c*1 (#15)] are predicted to be energetically more stable than  $\alpha$ -quartz. However, these phases have a very small stability pressure range (less than 0.4 GPa), and the  $\alpha$ -quartz phase transforms to the coesite-I phase SG *C*2/*c* at 3.1 GPa. The high-pressure phases of BeF<sub>2</sub> have been the subject of other first-principles calculations.<sup>10</sup> Very recently, first-principles calculations have also been employed to construct the *P*–*T* phase diagram of BeF<sub>2</sub>.<sup>11</sup> The HSE06 optical bandgap of the  $\alpha$ -quartz structure is found to be about 10.6 eV, and increases by increasing the applied pressure.<sup>9</sup> The lattice vibrations, inelastic scattering cross-sections, and neutron transmission of BeF<sub>2</sub> have been

<sup>a</sup>Institute of High Performance Computing, 1 Fusionopolis Way, #16-16 Connexis, 138632, Singapore. E-mail: ganck@ihpc.a-star.edu.sg

<sup>b</sup>Department of Physics, Yarmouk University, Irbid-21163, Jordan. E-mail: aqteish@yu.edu.jo


thoroughly investigated<sup>6</sup> using first-principles calculations and compared to those of MgF<sub>2</sub>.

The benchmark system ZnF<sub>2</sub> crystallizes in the tetragonal rutile structure with SG *P4<sub>2</sub>/mnm* (#136). Very recently, Raman scattering measurements with the use of the diamond anvil cell have been employed to investigate the structural phase transformations of ZnF<sub>2</sub> under high pressures.<sup>12</sup> This experimental work is supplemented by first-principles calculations. In addition to the structural stability and pressure variation of the Raman active phonon modes, the electronic bandgap of the considered phases as a function of pressure has been investigated at the HSE06 level. Neutron diffraction has been employed to study the temperature dependence of the lattice parameters and unit cell volume of ZnF<sub>2</sub>,<sup>13</sup> and NTE has been observed in a small temperature range (below 75 K). This NTE behavior has been supported by first-principles calculations.<sup>13,14</sup> However, only the volumetric TEC has been theoretically investigated.

In the present work, the linear TECs of BeF<sub>2</sub> and ZnF<sub>2</sub> are investigated by employing the recently introduced direct approach<sup>15</sup> in which the symmetry of the deformed structures could be preserved. Since this approach has not been applied to systems with tetragonal symmetry, ZnF<sub>2</sub> is thus chosen as a suitable benchmark system because of its tetragonal crystal structure, in addition to the existence of experimental and previous theoretical results of its volumetric thermal expansion. The elastic constants and phonon frequencies required to compute linear TECs are calculated from first-principles. For BeF<sub>2</sub>, the  $\alpha$ -quartz,  $\alpha$ -cristobalite and  $\alpha'$ -cristobalite phases will be considered. Moreover, the relative stability of the above three phases of BeF<sub>2</sub> are also investigated using different levels of approximation of the exchange-correlation potential.

## 2. Methodology

The linear TECs of the considered phases of ZnF<sub>2</sub> and BeF<sub>2</sub> are calculated within the Grüneisen formalism following the procedure described in ref. 16–22. To compute the mode Grüneisen parameters we considered two types of symmetry-preserving deformations obtained by changing the in-plane (*a*) or out-of-plane (*c*) lattice parameters by  $\pm 0.5\%$ . These deformations allow for the full utilization of the tetragonal or trigonal point-group symmetry<sup>23</sup> of the considered systems, which minimizes the required number of independent atomic displacements (*i.e.*, number of supercells) to calculate the phonon frequencies within the direct method.<sup>24–28</sup> The amplitude of atomic displacements, from the corresponding equilibrium positions, is 0.015 Å. The supercell sizes are of  $2 \times 2 \times 3$  for ZnF<sub>2</sub>, and  $2 \times 2 \times 2$  for the  $\alpha$ -quartz,  $\alpha$ -cristobalite, and  $\alpha'$ -cristobalite phases of BeF<sub>2</sub>. The adequacy of these supercells have been checked by considering larger ones for each of these systems, and we found that such actions do not alter appreciably our main results and conclusions. The determination of the linear TECs also requires the elastic constants that may be obtained through fittings of energy *versus* strain curves.<sup>29,30</sup> Specifically, these TECs at temperature *T* in the *a* ( $\alpha_a$ ) and *c* ( $\alpha_c$ ) directions of the above systems are given by

$$\begin{bmatrix} \alpha_a(T) \\ \alpha_c(T) \end{bmatrix} = \frac{1}{\Omega D} \begin{bmatrix} C_{33} & -C_{13} \\ -2C_{13} & (C_{11} + C_{12}) \end{bmatrix} \begin{bmatrix} I_a(T) \\ I_c(T) \end{bmatrix} \quad (1)$$

where  $C_{ij}$  are the elastic constants,  $D = (C_{11} + C_{12})C_{33} - 2C_{13}^2$  and  $\Omega$  is the volume of the primitive cell. The phonon density of states (PDOS) weighted by the Grüneisen parameters are

$$\Gamma_i(\nu) = \frac{\Omega}{(2\pi)^3} \sum_{\lambda} \int_{\text{BZ}} d\mathbf{q} \delta(\nu - \nu_{\lambda\mathbf{q}}) \gamma_{i,\lambda\mathbf{q}}, \quad (2)$$

with the Grüneisen parameter  $\gamma_{i,\lambda\mathbf{q}} = -\nu_{\lambda\mathbf{q}}^{-1} \partial \nu_{\lambda\mathbf{q}} / \partial \varepsilon_i$  for the deformation of type *i* (with *i* = *a* for in-plane and *i* = *c* for out-of-plane deformations). The derivative  $\partial \nu_{\lambda\mathbf{q}} / \partial \varepsilon_i$  measures the change of the frequency  $\nu_{\lambda\mathbf{q}}$  with respect to the strain parameter  $\varepsilon_i$ .<sup>15</sup> The summation is over all frequencies  $\nu_{\lambda\mathbf{q}}$  for the phonon band index  $\lambda$  and  $\mathbf{q}$  vector in the Brillouin zone (BZ). The  $I_i(T)$  are calculated from

$$I_i(T) = \int_{\nu_{\min}}^{\nu_{\max}} d\nu \Gamma_i(\nu) c(\nu, T) \quad (3)$$

where  $c(\nu, T) = k_B (r / \sinh r)^2$  is the contribution of the phonon modes with frequency  $\nu$  to the specific heat. Here,  $r = h\nu / 2k_B T$ , and  $h$  and  $k_B$  are the Planck and Boltzmann constants, respectively. The maximum (minimum) frequency is denoted by  $\nu_{\max}$  ( $\nu_{\min}$ ).

The DFT calculations of the optimized structural parameters, phonon frequencies, and elastic constants are performed by employing the projector augmented wave (PAW) method, as implemented in the Vienna *Ab Initio* Simulation Package (VASP). A relatively high cutoff energy of 600 eV is used for the plane-wave basis. Geometry optimization is stopped when the maximum force on each atom is less than  $10^{-3}$  eV Å<sup>-1</sup>. We find that phonon frequency shifts are more consistent when we use the local density approximation (LDA) for BeF<sub>2</sub>, and the PBE\_sol functional of the generalized gradient approximation (GGA) for ZnF<sub>2</sub>. Therefore, for the linear TECs only the results of these calculations are reported.

## 3. Results and discussion

### 3.1. Structural properties

We start with the benchmark system, ZnF<sub>2</sub>, which at ambient conditions crystallizes in the rutile structure, shown in Fig. 1(a). This crystal structure has a tetragonal symmetry and six atoms per primitive unit cell. The two Zn atoms occupy the Wyckoff 2a(0, 0, 0) sites and the four F atoms are located at the 4f(*x*, *x*, 0) sites. Therefore, this structure is characterized by three crystallographic parameters: two lattice parameters (*a* and *c*) and an internal parameter for the coordinates of the four F atoms (*x*). The structural parameters obtained using the PBE\_sol functional are (*a*, *c*, *x*) = (4.7194 Å, 3.1376 Å, 0.3037), while the corresponding LDA results are (4.6373 Å, 3.0990 Å, 0.3033). These calculated values are in very good agreement with the experimental data (4.7038 Å, 3.1336 Å, 0.3035)<sup>32</sup> and (4.7034 Å, 3.1335 Å, 0.303).<sup>13</sup> As expected, the LDA lattice parameters are underestimated while those of the PBE\_sol are slightly overestimated.



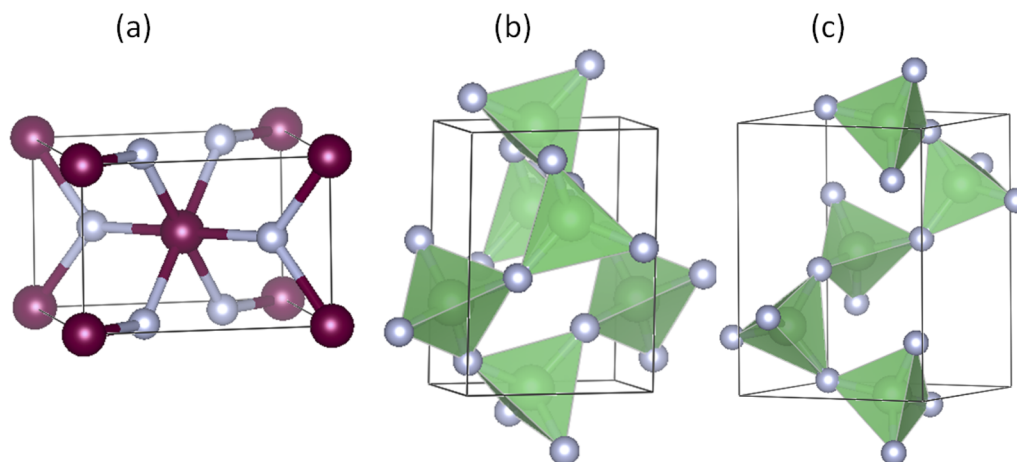


**Fig. 1** The crystal structures of (a) rutile  $\text{ZnF}_2$ , (b)  $\alpha$ -quartz  $\text{BeF}_2$ , and (c)  $\alpha$ -cristobalite  $\text{BeF}_2$ . The  $\alpha'$ -cristobalite  $\text{BeF}_2$  structure which is similar to the  $\alpha$ -cristobalite  $\text{BeF}_2$  structure is not shown. The small gray balls represent the F atoms. The  $c$  axis of the three crystal structures is along the vertical direction.

For  $\text{BeF}_2$ , the three considered crystal structures are  $\alpha$ -quartz [Fig. 1(b)],  $\alpha$ -cristobalite [Fig. 1(c)] and  $\alpha'$ -cristobalite. The  $\alpha$ -quartz phase has trigonal symmetry and nine atoms in the conventional hexagonal unit cell. The three Be atoms occupy the Wyckoff  $3a(x_1, x_1, 0)$  sites and the six F atoms occupy the  $6c(x_2, y_2, z_2)$  sites. On the other hand, the  $\alpha$ -cristobalite phase has a tetragonal symmetry and twelve atoms per primitive unit cell. The four Be atoms occupy the Wyckoff  $4a(x_1, x_1, 0)$  sites and the eight F atoms occupy the  $8c(x_2, y_2, z_2)$  sites. Therefore, each of these two structures has six crystallographic parameters: two lattice parameters ( $a$  and  $c$ ), and four internal parameters (denoted as  $x_1, x_2, y_2$  and  $z_2$ ). The atomic coordinates of the  $\alpha'$ -cristobalite phase can be obtained from those of the  $\alpha$ -cristobalite by mirror-image transformation  $(x, y, z) \rightarrow (-y, -x, z)$ , and the lattice parameters of the two structures are identical. Therefore, only the structure parameters of the first two crystal structures are reported. Our LDA, PBE<sub>sol</sub>, and PBE results, shown in Table 1, are in good agreement with available

experimental data and other theoretical calculations. The PBE<sub>sol</sub> results lie between the corresponding LDA and PBE results and show the best agreement with the experimental data for the  $\alpha$ -quartz.

### 3.2. Elastic properties and stability

We show in Table 1 the LDA, PBE<sub>sol</sub> and PBE relative energies ( $\Delta E$ ) of the  $\alpha$ -cristobalite phase with respect to those of  $\alpha$ -quartz. According to the PBE and PBE<sub>sol</sub> calculations the latter phase is slightly more stable, in accordance with the Nelson *et al.*<sup>9</sup> GGA calculations. However, the LDA calculations lead to an opposite conclusion. Similar conclusions have recently been reached by Masoumi,<sup>11</sup> using both LDA and GGA calculations. These results show that these two phases have extremely close cohesive energies.

The  $\alpha$ -quartz phase of  $\text{BeF}_2$  with a trigonal crystal symmetry has six independent elastic constants.<sup>34</sup> On the other hand, the rutile phase of  $\text{ZnF}_2$  and  $\alpha$ -cristobalite phase of  $\text{BeF}_2$  (both have

**Table 1** Calculated lattice constants and internal parameters of the  $\alpha$ -quartz and  $\alpha$ -cristobalite phases of  $\text{BeF}_2$ . Also shown are the relative energy ( $\Delta E$ ) of the  $\alpha$ -cristobalite phase with respect to that of  $\alpha$ -quartz, and the available experimental data (measured at 100 K) and other theoretical results

Phase	Approach	Lattice constants		Internal parameters				$\Delta E$ (meV)
		$a$ (Å)	$c$ (Å)	$x_1$	$x_2$	$y_2$	$z_2$	
$\alpha$ -Quartz	LDA	4.5958	5.0529	0.4579	0.4098	0.2867	0.2290	
	PBE <sub>sol</sub>	4.7301	5.1814	0.4662	0.4138	0.2737	0.2188	
	PBE	4.8497	5.3070	0.4756	0.4176	0.2575	0.2053	
	PBE <sup>6</sup>	4.8282	5.2837	0.4740	0.4171	0.2601	0.2075	
	LDA <sup>31</sup>	4.6663	5.1608					
	Expt. <sup>8</sup>	4.7390	5.1875	0.4700	0.4164	0.2671	0.2131	
$\alpha$ -Cristobalite	LDA	4.5967	6.1773	0.3226	0.2230	0.1454	0.2000	25
	PBE <sub>sol</sub>	4.8087	6.5984	0.3044	0.2378	0.1112	0.1825	−2
	PBE	4.8934	6.7428	0.2988	0.2400	0.1001	0.1769	−9
	LDA <sup>31</sup>	4.695	6.318					
	LDA <sup>11</sup>	4.684	6.373					
	PBE <sup>11</sup>	4.960	6.910					



Table 2 Calculated elastic constants of the  $\alpha$ -quartz and  $\alpha$ -cristobalite phases of BeF<sub>2</sub>, and the rutile phase of ZnF<sub>2</sub>

			Elastic constants (GPa)						
System	Phase	Approach	$C_{11}$	$C_{12}$	$C_{13}$	$C_{14}$	$C_{33}$	$C_{44}$	$C_{66}$
BeF <sub>2</sub>	$\alpha$ -Quartz	LDA	46.975	14.223	12.067	−6.401	75.287	31.745	
		PBE_sol	42.278	4.991	3.760	−9.077	53.009	30.548	
	$\alpha$ -Cristobalite	LDA	33.309	7.300	−5.087		22.487	35.810	13.731
		PBE_sol	32.589	4.839	−5.336		24.412	37.813	16.078
ZnF <sub>2</sub>	Rutile	LDA	139.442	121.550	109.127		220.673	36.583	91.826
		PBE_sol	128.470	98.717	94.547		200.902	35.523	83.001
		Expt. <sup>33</sup>	125.5	91.8	83.0		192.2	39.5	80.7

a tetragonal crystal symmetry) also have six independent elastic constants.<sup>34</sup> The elastic constants of these phases, obtained by using the LDA and PBE\_sol functionals are shown in Table 2. There are two features to note from this table. First, our results for the rutile ZnF<sub>2</sub> are in very good agreement with the available experimental values.<sup>33</sup> Secondly, the PBE\_sol values are systematically smaller than the corresponding LDA values, which is expected since the PBE\_sol GGA functional leads to softer materials than LDA (see above). The calculated elastic constants are used in the calculations of the linear TECs (see Sec. 2).

The elastic constants could be used to investigate the mechanical stability of the crystal structure. For  $\alpha$ -quartz structure, the Born stability criteria<sup>34</sup> are

$$D = (C_{11} + C_{12})C_{33} - 2C_{13}^2 > 0, \quad (4)$$

and

$$(C_{11} - C_{12})C_{44} - 2C_{14}^2 > 0. \quad (5)$$

Note that the same expression of  $D$  appears in eqn (1). As for the rutile and  $\alpha$ -cristobalite phases (of tetragonal (I) class),<sup>35</sup> the Born stability criteria are:  $C_{11} > |C_{12}|$ ,  $D > 0$ ,  $C_{44} > 0$  and  $C_{66} > 0$ . The elastic constants reported in Table 2 show that these criteria are satisfied, and therefore the considered phases of

ZnF<sub>2</sub> and BeF<sub>2</sub> are mechanically stable. The mechanical stability of these crystal structures can also be inferred from phonon dispersion relations, discussed below.

### 3.3. Phonon dispersion relations

Since the considered crystals are polar in character we perform non-analytical correction (NAC) to their dynamical matrices. To do that, we have calculated the high-frequency dielectric constant and Born effective charge tensors, and the results are listed in Table 3. The features to note from this table are the following. (i) The calculated results have a very weak dependence on the used exchange-correlation functional. (ii) The effective charges in the ZnF<sub>2</sub> are larger than in BeF<sub>2</sub>, which shows that the ionicity of Zn–F bond is larger than that in Be–F. This is consistent with the corrected Allred–Rochow electronegativity values<sup>39</sup> (larger for Be). (iii) Our calculated  $xx$  and  $yy$  components of the dielectric constant are in very good agreement with available experimental data,<sup>36</sup> while that of  $zz$  is larger than the measured one. However, the comparable values of diagonal components of the dielectric constant in our calculations are consistent with the experimental and calculated values for other metal fluorides crystallizing in the rutile structure (such as MgF<sub>2</sub> and FeF<sub>2</sub>).<sup>40</sup>

Fig. 2 shows the calculated phonon dispersion relations and PDOS of the rutile ZnF<sub>2</sub>, with and without NAC. Also shown are

Table 3 Calculated high-frequency dielectric constants (DCs) and Born effective charges of the  $\alpha$ -quartz (AQ) and  $\alpha$ -cristobalite (AC) phases of BeF<sub>2</sub>, and the rutile phase of ZnF<sub>2</sub>

System	Phase	Approach	DC		Atom	Born effective charge								
			$xx = yy$	$zz$		$xx$	$xy$	$xz$	$yx$	$yy$	$yz$	$zx$	$zy$	$zz$
BeF <sub>2</sub>	AQ	PBE_sol	1.902	1.912	Be	1.728	0.000	0.000	0.000	1.914	0.081	0.000	−0.079	1.866
					F	−0.747	0.221	−0.115	0.213	−1.074	0.337	−0.095	0.345	−0.933
		LDA	1.887	1.896	Be	1.727	0.000	0.000	0.000	1.918	0.080	0.000	−0.0758	1.864
					F	−0.746	0.226	−0.124	0.218	−1.076	0.343	−0.104	0.356	−0.932
BeF <sub>2</sub>	AC	PBE_sol	1.723	1.718	Be	1.832	0.005	−0.045	0.005	1.832	0.049	0.100	−0.101	1.810
					F	−1.221	−0.117	0.377	−0.101	−0.611	0.061	0.380	0.100	−0.905
		LDA	1.827	1.818	Be	1.823	0.005	−0.036	0.005	1.823	0.036	0.110	−0.110	1.790
					F	−1.199	−0.135	0.329	−0.120	−0.624	0.076	0.333	0.115	−0.896
ZnF <sub>2</sub>	Rutile	PBE_sol	2.549	2.664	Zn	2.222	−0.162	0.000	−0.162	2.222	0.00	0.000	0.000	2.424
					F	−1.111	−0.409	0.000	−0.409	−1.111	0.000	0.000	0.000	−1.200
		LDA	2.547	2.653	Zn	2.206	−0.1493	0.000	−0.1493	2.206	0.000	0.000	0.000	2.392
					F	−1.103	−0.395	0.000	−0.395	−1.103	0.000	0.000	0.000	−1.196
		Expt. <sup>36</sup>	2.6	2.1										



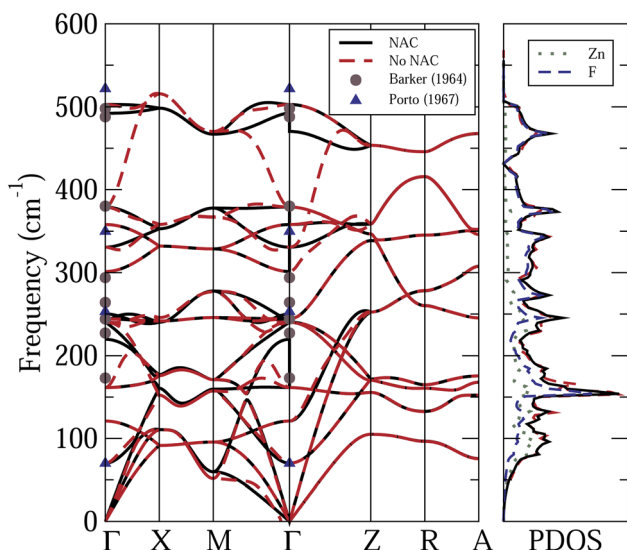


Fig. 2 Calculated phonon dispersion relations and PDOS of  $\text{ZnF}_2$ , with (black solid curves) and without (red dashed curves) non-analytic correction (NAC). The Zn and F projected PDOS, with NAC, and also shown. Symbols: available experimental data.<sup>37,38</sup>

the calculated Zn and F projected PDOS, with NAC, and the available experimental data.<sup>37,38</sup> The frequency spans across an interval of about  $500 \text{ cm}^{-1}$ . The features to note from this figure are the following. (i) As expected, the NAC leads to longitudinal optical-traverse optical (LO-TO) splitting, near the  $\Gamma$  point. The strongest effects are felt by high-frequency optical modes. However, the effects of the NAC on the calculated PDOS are quite small. (ii) Experimental data are available only for infrared<sup>37</sup> and Raman<sup>12,38</sup> active modes at the  $\Gamma$ -points. The reported frequencies of the latter modes are in very good agreement with each other, and hence only those of ref. 38 are shown in Fig. 2. For the designation of these phonon modes see ref. 40. Fig. 2 shows that these experimental data agree reasonably well with our first-principles results.

Fig. 3 shows the phonon dispersion relations of the  $\alpha$ -quartz and  $\alpha$ -cristobalite phases of  $\text{BeF}_2$ , taking into account the NAC. Also shown are the PDOS, and Be and F projected PDOS of the  $\alpha$ -cristobalite phase. The results of the  $\alpha'$ -cristobalite phase are very similar to those of  $\alpha$ -cristobalite and hence are not shown. The features to note from this figure are the following. (i) The very wide frequency range of the phonon modes in these systems, compared to that of  $\text{ZnF}_2$ . This can be understood as a consequence of the rather large mass difference between Be and Zn atoms. (ii) The frequency range of both phases of  $\text{BeF}_2$  can be separated, according to the character of the phonon modes, into three sub-regions. (a) The lower frequency region between 0 and about  $700 \text{ cm}^{-1}$ , where the phonon modes are mainly due to the vibrations of F atoms. The contribution of the Be atoms becomes appreciable above  $300 \text{ cm}^{-1}$ . It is worth noting that in the case of  $\text{ZnF}_2$  the dominance of the vibrations of the F atoms occurs in the upper part of the frequency range because the Zn atom is heavier than the F atom. (b) A narrow intermediate region at about  $770 \text{ cm}^{-1}$ , where the rather

localized phonon modes originate from vibrations involving both Be and F atoms. (c) The upper-frequency region, where the phonon modes originate mainly from vibrations of Be atoms. (iii) The opening of two frequency gaps, between (a) and (b), and between (b) and (c) sub-regions. These frequency gaps can be understood as a consequence of the localization of phonon modes in the (b) sub-region.

### 3.4. Thermal expansion

The calculated linear and volumetric TECs of the considered phases of  $\text{ZnF}_2$  and  $\text{BeF}_2$ , according to the procedure described in Sec. 2, are depicted in Fig. 4 and 5, respectively. It is worth mentioning that, as expected, the NACs to the dynamical matrices have negligible effects on the calculated linear TECs.

We will first look at the TECs of  $\text{ZnF}_2$ . The important features to note from Fig. 4 are the following. (i) The NTE at low temperatures is mostly due to  $\alpha_a$ . The negative values of  $\alpha_c$  are smaller (in magnitude) than those of  $\alpha_a$  and lie in a considerably shorter  $T$ -range. This is clear from the magnitude and the location of the minimum values:  $\alpha_a \sim -1.05 \times 10^{-6} \text{ K}^{-1}$  at 55 K, and  $\alpha_c \sim -0.5 \times 10^{-6} \text{ K}^{-1}$  at 40 K. These results are consistent with observed  $T$ -variations of the  $a$  and  $c$  lattice parameters at low temperatures (see Fig. 3 of ref. 13). (ii) The calculated  $\alpha_v$  from the linear TECs (*i.e.*,  $\alpha_v = 2\alpha_a + \alpha_c$ ) are in good agreement with the previous direct theoretical calculations,<sup>13,14</sup> and the results of all these theoretical calculations are in a qualitative agreement with experimental data.<sup>13</sup> This finding reflects the accuracy and reliability of our calculated linear TECs. (iii)  $\alpha_c$  is systematically and appreciably larger than  $\alpha_a$ . For example, at 300 K the calculated value of  $\alpha_c$  (of  $8.9 \times 10^{-6} \text{ K}^{-1}$ ) is about 60% larger than that of  $\alpha_a$  (of  $5.6 \times 10^{-6} \text{ K}^{-1}$ ).

As for the thermal expansion of the considered phases of  $\text{BeF}_2$ , the features to note from Fig. 5 are the following. (i) Unlike  $\text{ZnF}_2$ , the calculated values of both  $\alpha_a$  and  $\alpha_c$  are always positive for all of the considered phases of  $\text{BeF}_2$ . (ii) Both  $\alpha_c$  and  $\alpha_a$  of the  $\alpha$ -cristobalite structure are very close to those of  $\alpha'$ -cristobalite, and hence only those of the former phase will be discussed below. (iii) In the considered  $T$ -range,  $\alpha_a(T)$  of the  $\alpha$ -quartz structure is slightly larger than  $\alpha_c(T)$ , whereas  $\alpha_a(T)$  of the  $\alpha$ -cristobalite phase is much smaller than  $\alpha_c(T)$ . (iv) The large  $\alpha_c$  and  $\alpha_a$  lead to very large  $\alpha_v$  for both phases of  $\text{BeF}_2$ . For example, at 300 K, the values of  $\alpha_v$  are of  $77.6$  and  $169.9 \times 10^{-6} \text{ K}^{-1}$  respectively for the above two phases of  $\text{BeF}_2$ , compared to that of  $20.0 \times 10^{-6} \text{ K}^{-1}$  for  $\text{ZnF}_2$ . Our largest calculated linear TEC is of  $\sim 95 \times 10^{-6} \text{ K}^{-1}$  at 300 K for  $\alpha_c$  of the  $\alpha$ -cristobalite phase. This is indeed large compared to the experimental linear TECs at 300 K of four fluorites, *i.e.*,  $\text{CaF}_2$ ,  $\text{SrF}_2$ ,  $\text{BaF}_2$ , and  $\text{PbF}_2$  (ref. 41) that range between  $18.1$  and  $29 \times 10^{-6} \text{ K}^{-1}$ , but still is somewhat smaller than the measured linear TEC value of  $163.9 \times 10^{-6} \text{ K}^{-1}$  of an Ti-Nb alloy.<sup>42</sup>

The key physically insightful quantity for the interpretation of the above results is the PDOS weighted by the Grüneisen parameters,  $\Gamma_i(\nu)$ , defined in eqn (2). Fig. 6 shows  $\Gamma_i(\nu)$  of  $\text{ZnF}_2$ , and the  $\alpha$ -quartz and  $\alpha$ -cristobalite phases of  $\text{BeF}_2$ . The important features to note from this figure are the following. (i) For  $\text{ZnF}_2$ , the low-frequency modes ( $\nu < 150 \text{ cm}^{-1}$ ) have negative



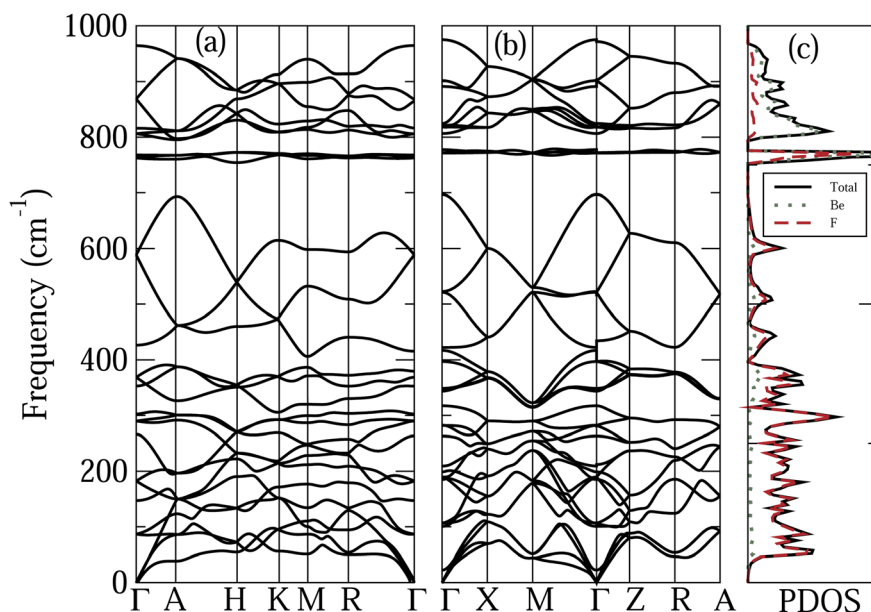


Fig. 3 Calculated phonon dispersion relations of the (a)  $\alpha$ -quartz and (b)  $\alpha$ -cristobalite phases of  $\text{BeF}_2$ . (c) PDOS, and the Be and F projected PDOS of the  $\alpha$ -cristobalite phase.

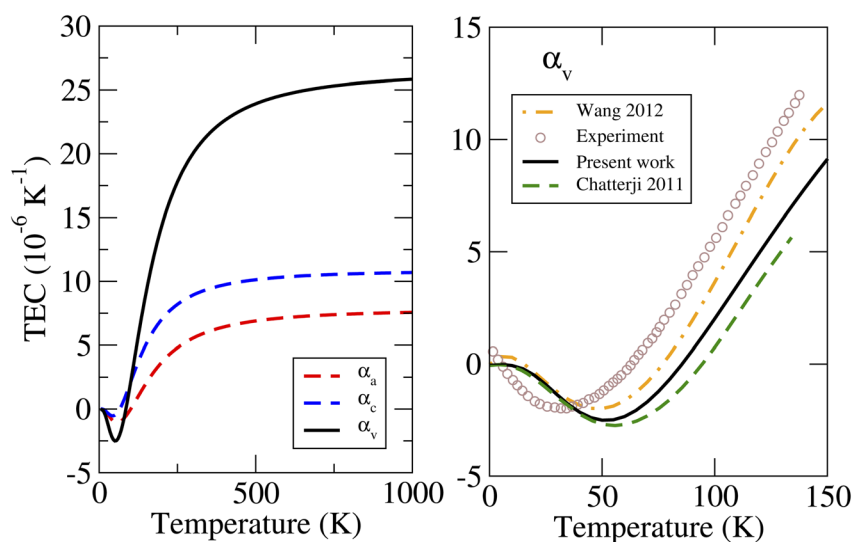


Fig. 4 Calculated linear and volumetric TECs of  $\text{ZnF}_2$  using the LDA, compared to the available experimental data<sup>13</sup> and previous theoretical results.<sup>13,14</sup>

Grüneisen parameters, which lead to negative  $\Gamma_i(\nu)$  in this  $\nu$  range. Since low-frequency modes are easily thermally excited, this finding explains the observed NTE in  $\text{ZnF}_2$ . Moreover, by inspecting the differences between  $\Gamma_a(\nu)$  and  $\Gamma_c(\nu)$  one can easily understand why  $\alpha_a$  is always lower than  $\alpha_c$ . (ii) The  $\Gamma_i(\nu)$  of the considered phases of  $\text{BeF}_2$  are always positive, which reflects the dominance of positive mode Grüneisen parameters in these phases. This explains the lack of NTE in the considered phases of  $\text{BeF}_2$ . (iii) The  $\Gamma_a(\nu)$  and  $\Gamma_c(\nu)$  of  $\alpha$ -quartz  $\text{BeF}_2$  have comparable magnitudes, with  $\Gamma_c(\nu)$  being smaller than  $\Gamma_a(\nu)$  for  $\nu < 100 \text{ cm}^{-1}$ , which explain the comparable magnitudes and

ordering of its  $\alpha_c$  and  $\alpha_a$ . (iv) The peak in  $\Gamma_c(\nu)$  of the  $\alpha$ -cristobalite phase around  $\nu \sim 34 \text{ cm}^{-1}$  is much higher than that of the  $\Gamma_a(\nu)$ , which results in a large  $\alpha_c$  compared to  $\alpha_a$ . This finding means that, in this  $\nu$ -range, the positive mode Grüneisen parameters associated with the out-of-plane deformation are significantly larger than those associated with the in-plane deformation. The large Grüneisen parameters can be viewed as a manifestation of strong anharmonic effects in the  $\alpha$ -cristobalite and  $\alpha'$ -cristobalite structures of  $\text{BeF}_2$ . However, it should be noted that large Grüneisen parameters are not the only factor that is responsible for the giant  $\alpha_v$  of the  $\alpha$ -

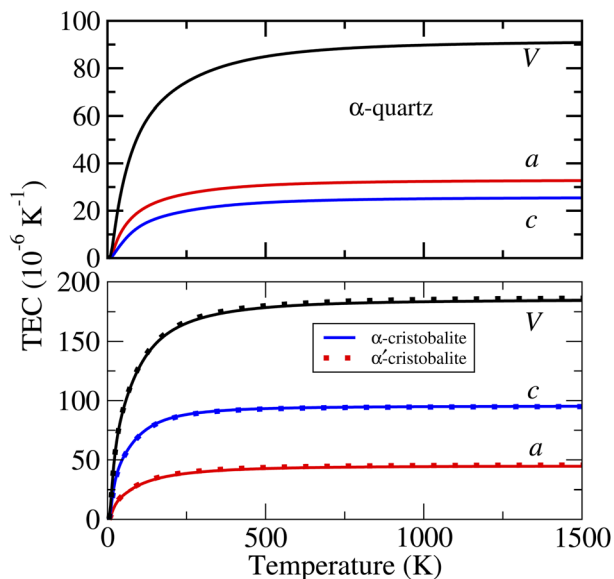


Fig. 5 Calculated linear and volumetric TECs with PBE\_sol of the three considered phases of BeF<sub>2</sub>. Note the difference in the scales of the two panels.

cristobalite: the elastic property *via* the negative (and with a large magnitude)  $C_{13}$  elastic constant (see Table 2 and eqn (1)) plays also a major role. The above findings explain the much larger volumetric TEC of the  $\alpha$ -cristobalite phase of BeF<sub>2</sub>, compared to that of the  $\alpha$ -quartz phase, which, in turn, is larger than that of ZnF<sub>2</sub>.

## 4. Summary

First-principles calculations are performed to investigate the structural, elastic, and vibrational properties of the rutile structure of ZnF<sub>2</sub> and three crystal structures of BeF<sub>2</sub> ( $\alpha$ -quartz,  $\alpha$ -cristobalite and its similar phase with space group  $P4_32_12$ ). The so-obtained phonon density of states, mode Grüneisen parameters, and elastic constants are used to study the linear thermal expansion coefficients (TECs) of the compounds mentioned above, within a Grüneisen formalism. We have used deformations that preserve the symmetry of the crystal to obtain the Grüneisen parameters. The considered crystal structures of both systems are found to be mechanically stable. The calculated physical quantities for both systems are in very good agreement with the available experimental data and previous theoretical results. For ZnF<sub>2</sub>, the calculated linear TECs,  $\alpha_a$  and  $\alpha_c$ , along the  $a$  and  $c$  directions are consistent with the experimental  $T$ -variations of the corresponding lattice parameters, respectively. The volumetric TEC  $\alpha_v$ , computed from these linear TECs is in qualitative agreement with experiment at low temperatures, including negative thermal expansion (NTE) behavior. The considered phases of BeF<sub>2</sub> are not NTE materials, and their linear TECs are much higher than those of ZnF<sub>2</sub>, especially for the  $\alpha$ -cristobalite phase. The elastic constants, high-frequency dielectric constants, Born effective charge tensors, and TECs of the considered phases of BeF<sub>2</sub> are reported in this work for the first time and could serve as predictions.

## Conflicts of interest

There are no conflicts to declare.

## Acknowledgements

We thank the National Supercomputing Center, Singapore (NSCC) and A\*STAR Computational Resource Center, Singapore (ACRC) for computing resources. We also thank Iyad Al-Qasir for fruitful discussions. This work is supported by RIE2020 Advanced Manufacturing and Engineering (AME) Programmatic grant no. A1898b0043.

## References

- 1 J. Parker and P. France, in *Glasses and glass-ceramics*, ed. M. H. Lewis, Chapman and Hall, 2011, p. 156.
- 2 F. Gan, Optical properties of fluoride glasses: a review, *J. Non-Cryst. Solids*, 1995, **184**, 9.
- 3 M. J. Weber, C. F. Cline, W. L. Smith, D. Milam, D. Heiman and R. Hellwarth, Measurements of the electronic and nuclear contributions to the nonlinear refractive index of beryllium fluoride glasses, *Appl. Phys. Lett.*, 1978, **32**, 403.
- 4 L. Mei, X. Cai, D. Jiang, J. Chen, W. Guo and W. Xiong, Investigation of thermal neutron scattering data for BeF<sub>2</sub> and LiF crystals, *J. Nucl. Sci. Tech.*, 2013, **50**, 419.
- 5 R. Kagawa, M. Montgomery, K. Braig, A. Leslie and J. Walker, The structure of bovine F<sub>1</sub>-ATPase inhibited by ADP and beryllium fluoride, *EMBO J.*, 2004, **23**, 2734.

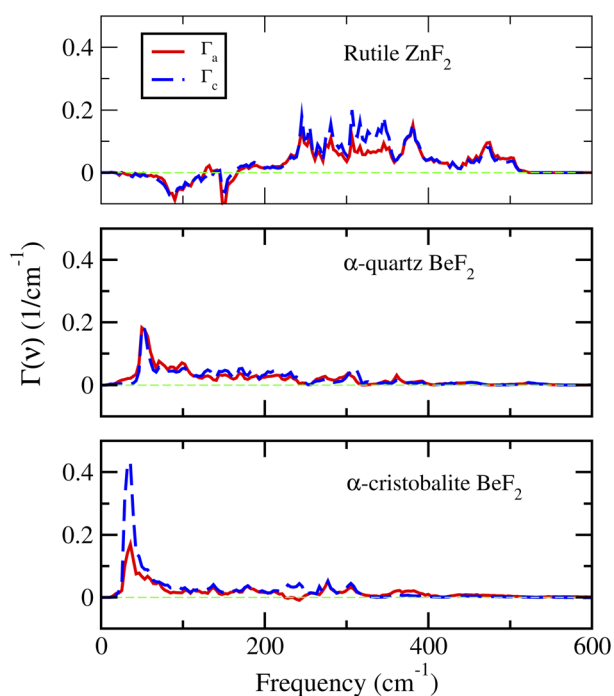


Fig. 6 The PDOS weighted by the Grüneisen parameters of the rutile ZnF<sub>2</sub>, and the  $\alpha$ -quartz and  $\alpha$ -cristobalite phases of BeF<sub>2</sub>.



- 6 I. Al-Qasir and A. Qteish, Neutron filter efficiency of beryllium and magnesium fluorides, *J. Appl. Crystallogr.*, 2017, **50**, 441.
- 7 Z. Kaawar and B. Paulus, A computational study of the structure of zinc fluoride surfaces, *AIP Conf. Proc.*, 2015, **1653**, 020051.
- 8 P. Ghalsasi and P. S. Ghalsasi, Single crystal X-ray structure of BeF<sub>2</sub>:  $\alpha$ -quartz, *Inorg. Chem.*, 2011, **50**, 86.
- 9 J. R. Nelson, R. J. Needs and C. J. Pickard, High-pressure phases of group II difluorides: polymorphism and superionicity, *Phys. Rev. B*, 2017, **95**, 054118.
- 10 M. S. Rakitin, A. R. Oganov, H. Niu, M. M. D. Esfahani, X.-F. Zhou, G.-R. Qian and V. L. Solozhenko, Novel phase of beryllium fluoride at high pressure, *Phys. Chem. Chem. Phys.*, 2015, **17**, 26283.
- 11 N. Masoumi, *First-principles DFT study of imide and fluoride analogs of silicon oxide, silicon oxynitride, and their alloys*, PhD thesis, Arizona State University, Cambridge, MA, 2021.
- 12 D. Kurzydowski, A. Oleksiak, S. B. Pillai and P. K. Jha, High-pressure phase transitions of zinc difluoride up to 55 GPa, *Inorg. Chem.*, 2020, **59**, 2584.
- 13 T. Chatterji, M. Zbiri and T. C. Hansen, Negative thermal expansion in znf<sub>2</sub>, *Appl. Phys. Lett.*, 2011, **98**, 181911.
- 14 L. Wang, P. -F. Yuan, F. Wang, Q. Sun, E. -J. Liang and Y. Jia, Theoretical study of negative thermal expansion mechanism of ZnF<sub>2</sub>, *Mater. Res. Bull.*, 2012, **47**, 1113.
- 15 C. K. Gan and K. T. E. Chua, Large thermal anisotropy in monoclinic niobium trisulfide: a thermal expansion tensor study, *J. Phys.: Condens. Matter*, 2019, **31**, 265401.
- 16 E. Grüneisen, *Handb. Phys.*, 1926, **10**, 1.
- 17 T. H. K. Barron, J. G. Collins and G. K. White, Thermal expansion of solids at low temperatures, *Adv. Phys.*, 1980, **29**, 609.
- 18 P. K. Schelling and P. Keblinski, Thermal expansion of carbon structures, *Phys. Rev. B: Condens. Matter Mater. Phys.*, 2003, **68**, 035425.
- 19 Y. Ding and B. Xiao, Thermal expansion tensors, Grüneisen parameters and phonon velocities of bulk MT<sub>2</sub> (M = W and Mo; T = S and Se) from first principles calculations, *RSC Adv.*, 2015, **5**, 18391.
- 20 C. K. Gan, J. R. Soh and Y. Liu, Large anharmonic effect and thermal expansion anisotropy of metal chalcogenides: the case of antimony sulfide, *Phys. Rev. B: Condens. Matter Mater. Phys.*, 2015, **92**, 235202.
- 21 G. Liu, H. M. Liu, J. Zhou and X. G. Wan, Temperature effect on lattice and electronic structures of WTe<sub>2</sub> from first-principles study, *J. Appl. Phys.*, 2017, **121**, 045104.
- 22 J. Liu and P. B. Allen, Internal and external expansions of wurtzite ZnO from first principles, *Comput. Mater. Sci.*, 2018, **154**, 251.
- 23 C. K. Gan, Y. Liu, T. C. Sum and K. Hippalgaonkar, Efficacious symmetry-adapted atomic displacement method for lattice dynamical studies, *Comput. Phys. Commun.*, 2021, **259**, 107635.
- 24 W. Frank, C. Elsässer and M. Fähnle, Ab initio force-constant method for phonon dispersions in alkali metals, *Phys. Rev. Lett.*, 1995, **74**, 1791.
- 25 K. Parlinski, Z. Q. Li and Y. Kawazoe, First-principles determination of the soft mode in cubic ZrO<sub>2</sub>, *Phys. Rev. Lett.*, 1997, **78**, 4063.
- 26 G. Kresse, J. Furthmüller and J. Hafner, Ab initio force constant approach to phonon dispersion relations of diamond and graphite, *Europhys. Lett.*, 1995, **32**, 729.
- 27 C. K. Gan, X. F. Fan and J. -L. Kuo, Composition-temperature phase diagram of Be<sub>x</sub>Zn<sub>1-x</sub>O from first principles, *Comput. Mater. Sci.*, 2010, **49**, S29.
- 28 Y. Liu, K. T. E. Chua, T. C. Sum and C. K. Gan, First-principles study of the lattice dynamics of Sb<sub>2</sub>S<sub>3</sub>, *Phys. Chem. Chem. Phys.*, 2014, **16**, 345.
- 29 A. Dal Corso, Elastic constants of beryllium: a first-principles investigation, *J. Phys.: Condens. Matter*, 2016, **28**, 075401.
- 30 C. K. Gan and C. H. Lee, Anharmonic phonon effects on linear thermal expansion of trigonal bismuth selenide and antimony telluride crystals, *Comput. Mater. Sci.*, 2018, **151**, 49.
- 31 F. Yu, M. Xu, M. Jiang and J. -X. Sun, The phase transitions and electronic structures of crystalline BeF<sub>2</sub> under high-pressure: First-principle calculations, *Solid State Commun.*, 2013, **169**, 14.
- 32 N. O'Toole and V. Streltsov, Synchrotron X-ray analysis of the electron density in CoF<sub>2</sub> and ZnF<sub>2</sub>, *Acta Cryst. B*, 2001, **57**, 128.
- 33 D. S. Rimai, Elastic properties of ZnF<sub>2</sub> between 4.2 and 300 K, *Phys. Rev. B: Solid State*, 1977, **16**, 4069.
- 34 W. Pabst and E. C. Gregorová, Elastic properties of silica polymorphs – a review, *Ceram.-Silik.*, 2013, **57**, 167.
- 35 F. Mouhat and F. -X. Coudert, Necessary and sufficient elastic stability conditions in various crystal systems, *Phys. Rev. B: Condens. Matter Mater. Phys.*, 2014, **90**, 224104.
- 36 R. E. Alaoui-Bichri, J. Giordano, R. Almairac, C. Benoit and P. Nassiri, Properties, *J. Phys.*, 1980, **41**, 543.
- 37 J. A. S. Barker, Transverse and longitudinal optic mode study in MgF<sub>2</sub> and ZnF<sub>2</sub>, *Phys. Rev.*, 1964, **136**, A1290.
- 38 S. P. S. Porto, P. A. Fleury and T. C. Damen, Raman spectra of TiO<sub>2</sub>, MgF<sub>2</sub>, ZnF<sub>2</sub>, FeF<sub>2</sub>, and MnF<sub>2</sub>, *Phys. Rev.*, 1967, **154**, 522.
- 39 A. Qteish, Electronegativity scales and electronegativity-bond ionicity relations: a comparative study, *J. Phys. Chem. Solids*, 2019, **124**, 186.
- 40 C. Benoit and J. Giordano, Dynamical properties of crystals of MgF<sub>2</sub>, ZnF<sub>2</sub> and FeF<sub>2</sub>. II. Lattice dynamics and infrared spectra, *J. Phys. C: Solid State Phys.*, 1988, **21**, 5209.
- 41 R. B. Roberts and G. K. White, Thermal expansion of fluorites at high temperatures, *J. Phys. C: Solid State Phys.*, 1986, **19**, 7167.
- 42 M. Bönisch, A. Panigrahi, M. Stoica, M. Calin, E. Ahrens, M. Zehetbauer, W. Skrotzki and J. Eckert, Giant thermal expansion and  $\alpha$ -precipitation pathways in Ti-alloys, *Nat. Commun.*, 2017, **8**, 1429.

